

MATERIALS SCIENCE

A pressure-induced topological phase with large Berry curvature in $\text{Pb}_{1-x}\text{Sn}_x\text{Te}$ Tian Liang,^{1*} Satya Kushwaha,² Jinwoong Kim,³ Quinn Gibson,^{2†} Jingjing Lin,¹ Nicholas Kioussis,³ Robert J. Cava,² N. Phuan Ong^{1‡}

2017 © The Authors, some rights reserved; exclusive licensee American Association for the Advancement of Science. Distributed under a Creative Commons Attribution NonCommercial License 4.0 (CC BY-NC).

The picture of how a gap closes in a semiconductor has been radically transformed by topological concepts. Instead of the gap closing and immediately reopening, topological arguments predict that, in the absence of inversion symmetry, a metallic phase protected by Weyl nodes persists over a finite interval of the tuning parameter (for example, pressure P). The gap reappears when the Weyl nodes mutually annihilate. We report evidence that $\text{Pb}_{1-x}\text{Sn}_x\text{Te}$ exhibits this topological metallic phase. Using pressure to tune the gap, we have tracked the nucleation of a Fermi surface droplet that rapidly grows in volume with P . In the metallic state, we observe a large Berry curvature, which dominates the Hall effect. Moreover, a giant negative magnetoresistance is observed in the insulating side of phase boundaries, in accord with *ab initio* calculations. The results confirm the existence of a topological metallic phase over a finite pressure interval.

INTRODUCTION

Topological concepts have greatly clarified the role of symmetry in protecting electronic states in a host of materials. In bulk semiconductors, topological insights have revised the picture of how the energy gap closes (say, under pressure P). In the old picture, the gap Δ closes at an “accidental” value of P before reopening at higher P . The new view (1–4) predicts instead that, when inversion symmetry is broken, a gapless metallic state featuring pairs of Weyl nodes persists over a field interval ($P_1 \rightarrow P_2$). They act as sources and sinks of Berry curvature (an effective magnetic field in \mathbf{k} space). The metallic phase is protected because the nodes come in pairs with opposite chiralities ($\chi = \pm 1$). Hence, they cannot be removed except by mutual annihilation (which eventually occurs at the higher pressure P_2). To date, these predictions have not been tested.

Here, we show that $\text{Pb}_{1-x}\text{Sn}_x\text{Te}$ exhibits a pressure-induced metallic phase described by the Weyl scenario. The Pb-based rock salts (5–7) have been identified as topological crystalline insulators with surface states protected by mirror symmetry (8–12). We focus on their Dirac-like bulk states (13, 14), which occur at the L points of the Brillouin zone (BZ) surface. $\text{Pb}_{1-x}\text{Sn}_x\text{Te}$ exhibits an insulator-to-metal (IM) transition at $P \sim 10$ kbar (7). However, the IM transition is little explored. We report that the metallic state appears by nucleating 12 small Fermi surface (FS) nodes. The breaking of time-reversal symmetry (TRS) in applied \mathbf{B} leads to a large Berry curvature Ω . Finally, we also observe an anomalously large negative magnetoresistance (MR), which is anticipated in the Weyl scenario.

RESULTS

Phase diagram under pressure

Crystals of $\text{Pb}_{1-x}\text{Sn}_x\text{Te}$ were grown by the vertical Bridgman technique (see Materials and Methods). Transport measurements at temperatures T down to 2 K were carried out in a Be-Cu pressure cell (with a max-

imum pressure of $P_{\text{max}} \sim 28$ kbar) on four samples with Sn contents $x = 0.5$ (samples A1 and A2), 0.32 (Q1), and 0.25 (E1) (Table 1). In A1 and A2, indium (6%) was added to tune the chemical potential (see Materials and Methods).

Figure 1 provides an overview of the IM transitions in samples A2 and E1. As P increases from 0 kbar (ambient pressure) to 25.4 kbar, the resistivity profile ρ versus T changes from insulating to metallic behavior in A2 (Fig. 1A). Close examination reveals a kink in ρ , indicating a sharp transition at $T_c = 62$ to 70 K (arrows in inset). Figure 1B shows the rapid increase in the zero- B conductivity $\sigma \equiv 1/\rho$ at 5 K as P exceeds the critical value $P_1 \sim 15$ kbar at the IM transition. The resistivity curves in sample E1 ($x = 0.25$) are broadly similar except that ρ at ambient P attains much higher values at 5 K ($3 \times 10^4 \Omega \text{ cm}$). As P increases from ambient to P_1 (12 kbar), an IM transition occurs to a metallic state (with ρ decreasing by over seven decades at 5 K). In samples E1 and Q1 (which have smaller Sn content than A1 and A2), the second critical pressure $P_2 = 25$ kbar is accessible in our experiment. The profile of σ versus P at 5 K (Fig. 1D) shows the metallic phase sandwiched between the two insulating phases.

The end member SnTe is known to be ferroelectric (FE) (15), but the existence of FE distortion is less obvious for finite Pb content. To establish inversion symmetry breaking, we performed dielectric measurements (see Materials and Methods) on sample E1, which has a very large ρ below 10 K ($>10^3 \Omega \text{ cm}$). By varying the E -field (12 \rightarrow 100 V/cm), we show that a large spontaneous dielectric response $\epsilon_1 \sim 5 \times 10^4$ exists in the limit $E \rightarrow 0$ (Fig. 1C, inset). The spontaneous polarization \mathbf{P}_s provides direct evidence that the insulating state below P_1 in E1 is FE. Although dielectric measurements cannot be performed in A2 (carrier screening is too strong), the kink in ρ (arrow) implies that \mathbf{P}_s appears at 62 to 70 K.

In parallel, we performed *ab initio* calculations (see details in the Supplementary Materials), in which the lattice parameter a is varied to simulate pressure. To break inversion symmetry, we assumed a weak FE displacement $\mathbf{d} \parallel [111]$. The calculations reveal that, above P_1 , two pairs of Weyl nodes appear near each of the points L_1 , L_2 , and L_3 (these are equivalent in zero B ; see Fig. 1, E and F). As P increases, the 12 nodes trace out elliptical orbits (shown expanded by a factor of 10 relative to the BZ caliper) and eventually annihilate pairwise (indicated by black dots), consistent with the scenario described by Murakami (2) and Murakami and Kuga (3). The red and blue arcs refer to nodes with

¹Department of Physics, Princeton University, Princeton, NJ 08544, USA. ²Department of Chemistry, Princeton University, Princeton, NJ 08544, USA. ³Department of Physics and Astronomy, California State University Northridge, Northridge, CA 91330, USA. *Present address: Department of Applied Physics, Stanford University, Stanford, CA 94305, USA.

†Present address: Department of Chemistry, University of Liverpool, Liverpool L69 3BX, UK.

‡Corresponding author. Email: npo@princeton.edu

$\chi = 1$ and -1 , respectively. The splitting of the node at L_0 occurs in a much narrower pressure interval.

Quantum oscillations

The samples' high mobilities μ (20,000 to 4×10^6 cm^2/Vs ; see Table 1) allow us to "count" the number of FS pockets by monitoring the Shubnikov–de Haas (SdH) oscillations. As shown in Fig. 1 (B and D), σ increases steeply with the reduced pressure $\Delta P = P - P_1$. Figure 2A

shows the resistivity ρ_{xx} measured in sample A2 in a transverse magnetic field \mathbf{B} ($\parallel \hat{z}$) at selected values of P . From the linear variation of $1/B_n$ versus the integers n (where B_n is the peak field in ρ_{xx} ; see Fig. 2B), we find that the FS caliper area S_F increases from 1.6 to 2.7 T between 19 and 25.4 kbar. The most prominent peak in Fig. 2A corresponds to the $n = 1$ Landau level (LL). The SdH-derived Fermi wave vector k_F corresponds to a hole density $p_{\text{SdH}} = \frac{4}{3}\pi k_F^3 / (2\pi)^3$ per spin (assuming a spherical FS).

The sharp increase in hole density is also evident in the Hall resistivity ρ_{yx} (which is B -linear in weak B). To highlight its behavior, we plot the ratio ρ_{yx}/Be versus B (Fig. 2C). In weak B (for example, $|B| < 3.5$ T in the top curve), the ratio is B -independent, which allows the ratio to be identified with the Hall density n_H (the abrupt increase above 3 T arises from the interesting anomalous Hall term discussed below). From n_H , we derive $\mu \sim 1.8 \times 10^4$ and 2.86×10^4 cm^2/Vs in A1 and A2, respectively, at 25 kbar.

Crucially, we find that n_H always exceeds p_{SdH} by an order of magnitude. This implies a large number N_F of identical pockets. The ratio $n_H/p_{\text{SdH}} = N_F$ equals 12 ± 1 over the whole pressure interval (Fig. 2B, inset). Because a smaller N_F (for example, 4, 6, or 8) can be excluded, the results strongly support the choice $\mathbf{d} \parallel [111]$, which leads to three equivalent L points.

Anomalous Hall effect

We next describe the evidence for a topological metallic phase. The Hall resistivity ρ_{yx} displays a highly unusual field profile. As B

Table 1. Parameters of samples of $\text{Pb}_{1-x}\text{Sn}_x\text{Te}$ investigated. Columns 2, 3, 4, and 5 report the Sn content x , the mobility μ , the Hall carrier density n_H , and the conductivity σ (at $B = 0$), respectively. The minus sign in n_H (sample Q1) indicates n -type carriers. All quantities in the table were measured at 5 K at the pressure P given in the last column. Samples A1 and A2 are slightly doped with In to tune the chemical potential [composition $(\text{Pb}_{0.5}\text{Sn}_{0.5})_{1-y}\text{In}_y\text{Te}$, with the In content $y = 0.06$].

Sample	x	μ (cm^2/Vs)	n_H (cm^{-3})	σ ($\text{m}\Omega \text{ cm}^{-1}$)	P (kbar)
A1	0.5	18,000	1.59×10^{17}	0.41	25
A2	0.5	29,000	1.56×10^{17}	0.68	25.4
E1	0.25	500,000	9.35×10^{15}	0.70	21.7
Q1	0.32	4.2×10^6	-1.05×10^{16}	7.02	21

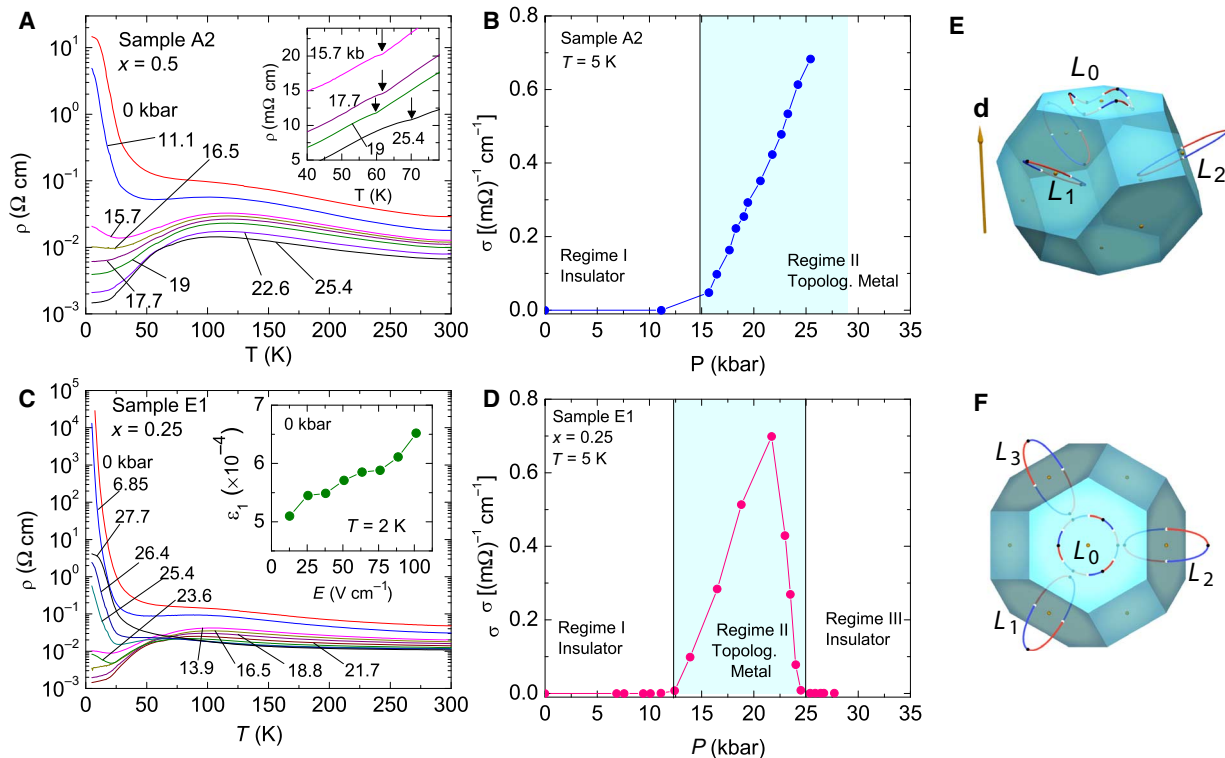


Fig. 1. The phase diagram of $\text{Pb}_{1-x}\text{Sn}_x\text{Te}$ inferred from the resistivity ρ versus temperature T and pressure P . (A) Curves of ρ versus T in sample A2 ($x = 0.5$) in zero B measured at selected P . At 5 K, ρ decreases by four orders of magnitude as $P \rightarrow 25.4$ kbar (the IM transition). The inset shows the kinks (arrows) in ρ (between 62 and 70 K), which signal a transition to a state with broken inversion symmetry. (B) Steep increase of the conductivity $\sigma = 1/\rho$ at 5 K in the metallic phase (shaded in blue; $P > P_1$). (C) ρ versus T at selected P in sample E1 ($x = 0.25$). The insulating state is recovered at $P_2 \sim 25$ kbar. The inset plots the dielectric response ϵ_1 measured versus applied electric field E at 2 K and ambient P (a spontaneous value $\epsilon_1 \sim 5 \times 10^4$ is measured as $E \rightarrow 0$). (D) σ versus P at 5 K to display the metallic state in E1 (shaded in blue) sandwiched between P_1 and P_2 . (E and F) Calculated Weyl node trajectories (Supplementary Materials), magnified 10 \times relative to the BZ scale (with $\mathbf{B} = 0$). In (E), the vector $\mathbf{d} \parallel [111]$ (arrow) is the assumed FE displacement. (F) Top view (sighting $\parallel \mathbf{d}$). Under pressure, the 12 Weyl nodes at L_1 , L_2 , and L_3 trace out elliptical orbits until they annihilate at the black points. The Weyl nodes at L_0 trace an orbit that undulates about a circular path [over a restricted pressure interval (Supplementary Materials)].

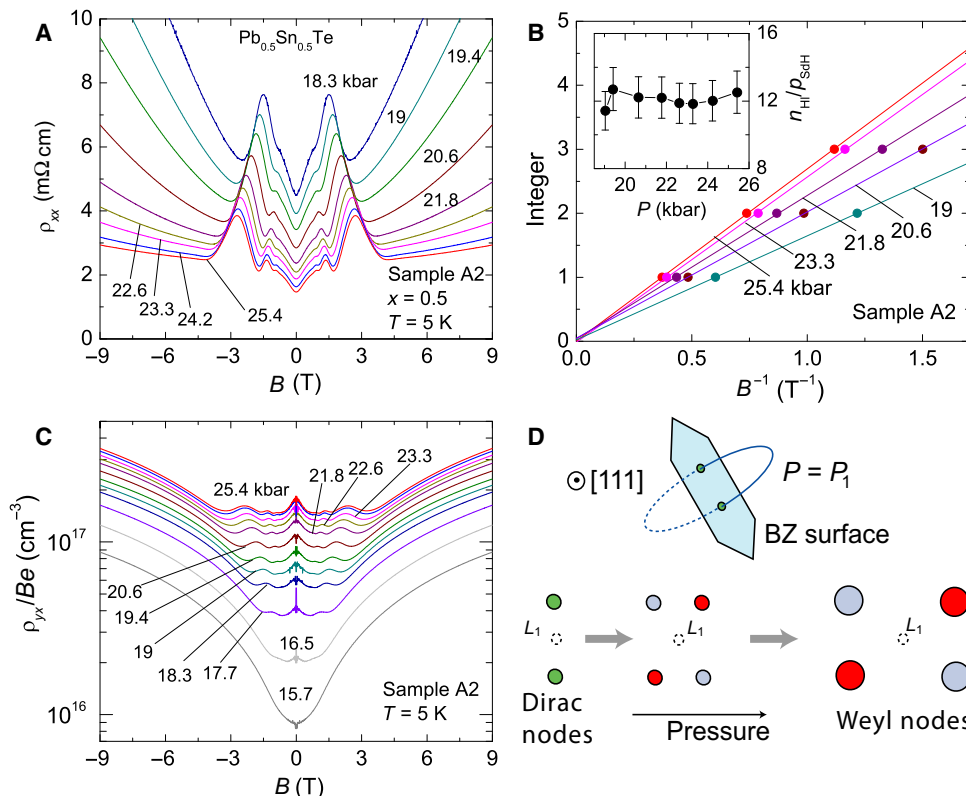


Fig. 2. The nucleation of small FS pockets above P_1 observed by SdH oscillations. (A) Resistivity ρ_{xx} versus a transverse B measured at 5 K and with P fixed at values 18.3 to 25.4 kbar (sample A2). At each P , the oscillations below 3 T correspond to SdH oscillations (the largest peak corresponds to the $n = 1$ LL). (B) Inverse peak fields $1/B_n$ of ρ_{xx} versus the integers n . The slopes yield small extremal FS cross sections S_F (1.6 to 2.7 T), which increase with $\Delta P = P - P_1$. The inset shows that the ratio n_H/ρ_{SdH} equals 12 ± 1 , independent of P (see text). (C) Hall resistivity (divided by Be) ρ_{yx}/Be versus B . At low B (where SdH oscillations occur), the flat profile allows ρ_{yx}/Be to be identified with the total hole density n_H . The strong increase in ρ_{yx}/Be above 3 T reflects the Berry curvature term (Fig. 3). (D) Top-down view (along $[\bar{1}\bar{1}1]$) of the L_1 hexagon face in zero B . At P_1 , two Dirac nodes nucleate around L_1 because of inversion-symmetry breaking. With increasing P , the four Weyl FS near L_1 move apart and expand in volume [chirality $\chi = 1$ (red) and -1 (gray)].

increases, the initial B -linear behavior abruptly changes, bending over to a nominally flat profile (Fig. 3A). At first glance, this recalls the anomalous Hall effect (AHE) in a ferromagnet (16) where the intrinsic AHE arises from a large Berry curvature rendered finite by the spontaneous breaking of TRS, but there is a subtle difference. In PbSnTe, TRS remains unbroken under P , so the AHE should be absent in the Weyl phase if $B = 0$ (Ω cancels pairwise between Weyl nodes with $\chi = \pm 1$). However, when TRS is broken in field B , the cancellation is spoiled by the Zeeman energy (see below). The field Ω leads to a large AHE signal. We remark that, in weak B (with Ω negligible), the initial slope of ρ_{yx} is dominated by the ordinary Hall effect, as evidenced by the linearity of n_H versus ρ_{SdH} in Fig. 2B [by contrast, in a ferromagnet, the AHE term is dominant even in weak B , so the weak- B ρ_{yx} and n_H are unrelated (16)].

The total (observed) Hall conductivity σ_{xy} is the sum of the conventional Hall and anomalous Hall conductivities, σ_{xy}^N and σ_{xy}^A , respectively (Fig. 3B). With σ_{xy}^N given by the Drude expression, we find that a good fit to σ_{xy} is achieved if we assume $\sigma_{xy}^A = \sigma_{AHE}^0 g(x)$, where σ_{AHE}^0 is the AHE amplitude and $g(x)$ is the smoothed step function $1/(e^{-x} + 1)$, with x being a reduced field (Supplementary Materials). In terms of Ω , σ_{AHE}^0 is given by (16)

$$\sigma_{AHE}^0 = \frac{e}{(2\pi)^3} \int d^3k \Omega_z(\mathbf{k}) f_{\mathbf{k}}^0 = e \langle \Omega_z \rangle n_{\text{tot}} \quad (1)$$

where $f_{\mathbf{k}}^0$ is the Fermi-Dirac distribution, $\langle \Omega_z \rangle$ is the Berry curvature averaged over the FS, and n_{tot} is the total carrier density. From the fits at each P , we can track the variation of $\langle \Omega_z \rangle \sim \sigma_{AHE}^0/n_{\text{tot}}$ versus P . As shown in

Fig. 3C, the curvature $\langle \Omega_z \rangle$ is negligible below P_1 but becomes large in the metallic phase, consistent with the Weyl scenario.

In Fig. 3B, we plot the observed σ_{xy} (solid curves) together with the Drude curve for σ_{xy}^N (dashed curves). Their difference is σ_{xy}^A (shaded region in the curve at 25 kbar). Similar results are obtained in A2 and E1 (Supplementary Materials). σ_{xy}^A grows quite abruptly at an onset field B_A close to where the system enters the lowest ($n = 0$) LL. Above B_A , the increasing dominance of the AHE current accounts for the abrupt bending of ρ_{yx} already noted in Fig. 3A, as well as the sharp increase above B_A in ρ_{yx}/Be in Fig. 2C. The observation that σ_{xy}^A is most prominent within the $n = 0$ LL (which is strictly chiral for Weyl fermions) suggests to us that it is intimately related to the chirality of the nodes.

Each Weyl node acts as a source ($\chi = 1$) or sink ($\chi = -1$) of Ω . As mentioned, in zero B , TRS requires the net sum of Ω over each pair of Weyl nodes to vanish (Fig. 3D). The ab initio calculations (Supplementary Materials) reveal how this cancellation is spoiled when TRS is broken in finite field B . A finite Zeeman field λ shifts the band energies, depending on their spin texture. This increases the \mathbf{k} -space separation and Fermi energy of one pair of nodes, say w_1^\pm , while reducing them in the other w_2^\pm (Fig. 3D). The unbalancing creates a finite Ω (hence, σ_{xy}^A) that grows with B (Supplementary Materials).

Giant MR

Perhaps the most marked feature in $Pb_{1-x}Sn_xTe$ is the appearance of giant negative MR at pressures just above P_2 . In Fig. 4A, we show the

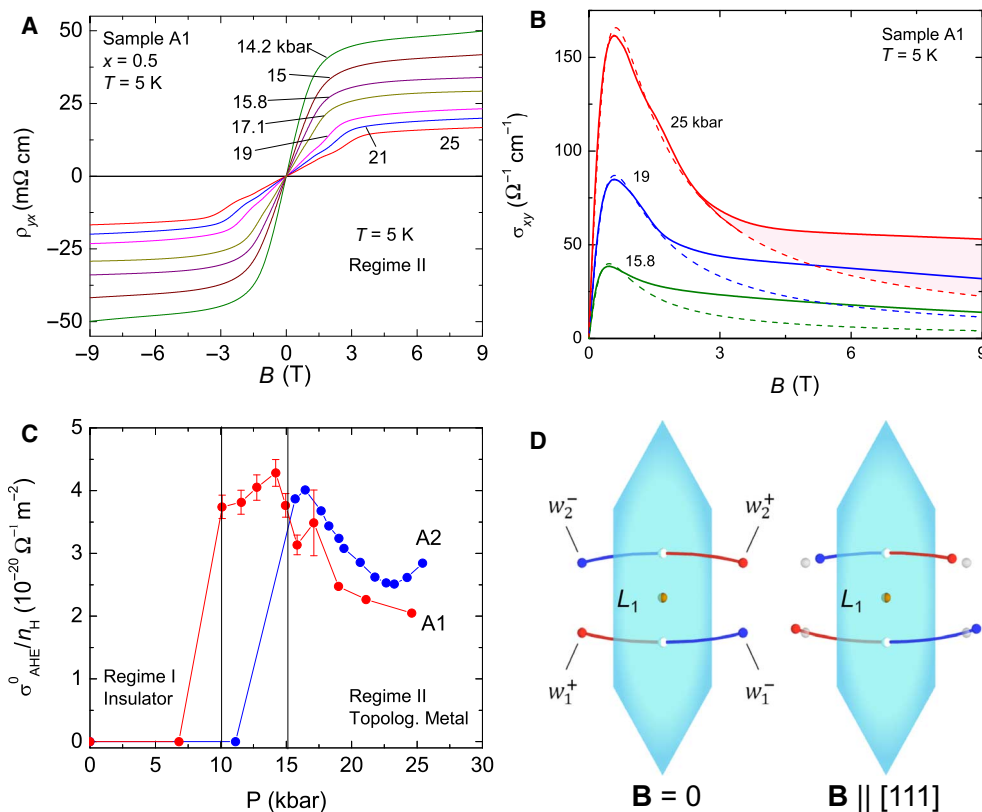


Fig. 3. The Berry curvature term in the Hall response. (A) Observed curves of ρ_{yx} versus B at 5 K with P fixed at values above P_1 . Instead of the conventional B -linear profile, ρ_{yx} bends over at low B (2 to 3 T), implying an extraordinary contribution to σ_{xy} at large B . (B) σ_{xy} versus B (derived from the measured ρ_{ij}) at three values of P . The Drude expression fits well to the curves at low B but reveals an excess contribution (shaded in the curve at 25 kbar) at large B , identified with σ_{xy}^A , that increases with B . (C) Ratio σ_{xy}^A/n_H (see fits in the Supplementary Materials) versus P in samples A1 and A2 ($x = 0.5$). The ratio, which is proportional to $\langle \Omega_z \rangle$, shows a sharp increase at P_1 , followed by a milder variation in the metallic phase. (D) Effect of B on the Weyl node separations (viewed along $[\bar{1}\bar{1}1]$). In zero B (left), the Weyl nodes are equal in size and symmetrically located about L_1 (Ω vanishes). A finite Zeeman field (right) increases the separation and Fermi energy of the pair w_1^+ while decreasing them in w_2^- . The explicit breaking of TRS leads to a finite σ_{xy}^A .

MR curves in sample Q1 for selected T with P fixed at 28 kbar (roughly 3 kbar above P_2). At 4.3 K, ρ_{xx} decreases by a factor of 30 as B increases to 10 T (aside from a slight dip feature below 0.5 T). In Fig. 4B, similar curves for E1 (at pressure $P = 25.4$ kbar) show an even larger negative MR (the weak- B dip feature is more prominent as well). The large negative MR is steadily suppressed as we increase P beyond the P_2 boundary. The negative MR magnitude is similar in magnitude in both the transverse MR and longitudinal MR geometries ($B \parallel \hat{z}$ and $B \parallel \hat{x}$, respectively). This implies a Zeeman spin mechanism. Finally, we note that, in both Q1 and E1, ρ_{xx} measured at 10 T decreases as $T \rightarrow 5$ K (that is, the system is metallic).

DISCUSSION

The anomalously large changes in ρ_{xx} imply that the insulating state (at zero B) is converted to a metallic state in finite B . This is confirmed in the ab initio calculation (Supplementary Materials). A large λ favors the Weyl phase (the left V-shaped yellow region in Fig. 4C). As the phase boundary now tilts into the insulating side, the metallic phase is reentrant in increasing B . The observation of the giant negative MR provides further evidence in support of the Weyl node scenario.

As predicted in previous studies (1–4), gap closing in materials lacking inversion symmetry leads to a metallic phase that is protected by the distinct chirality of Weyl nodes. $\text{Pb}_{1-x}\text{Sn}_x\text{Te}$ is an instructive first

example. Increasing pressure P drives an IM transition at P_1 , with ρ (at 5 K) falling by four to seven orders of magnitude. Above P_1 , the growth of the FS calipers is tracked by large SdH oscillations. The number of nodes (12) is consistent with the appearance of four Weyl nodes at each of the 3 L_1 points on the BZ surface. The Berry curvature, rendered finite in B , leads to an AHE that is most prominent in the $n = 0$ LL. Finally, we find that the boundary P_2 is shifted in finite B . The reentrance of the metallic phase leads to a marked decrease in ρ_{xx} by a factor of 30 to 50.

MATERIALS AND METHODS

Crystal growth

Single crystals of $\text{Pb}_{1-x}\text{Sn}_x\text{Te}$ were grown by the conventional vertical Bridgman technique. High-purity elements (5N) with the targeted values of x were sealed in carbon-coated quartz tubes under a high vacuum of $\sim 10^{-5}$ mbar. The ampoules were heated at 1050°C for 12 hours. To ensure homogeneous mixing of the melt and to avoid bubble formation in the bottom, we stirred the ampoules. The ampoules were slowly lowered through the crystallization zone of the furnace, at the rate of 1 mm/hour. High-quality single-crystal boules of length ~ 10 cm were obtained. The crystal boules were cut into segments of 1 cm to investigate the bulk electronic properties along the boule length. The crystals were easily cleavable along different crystallographic planes.

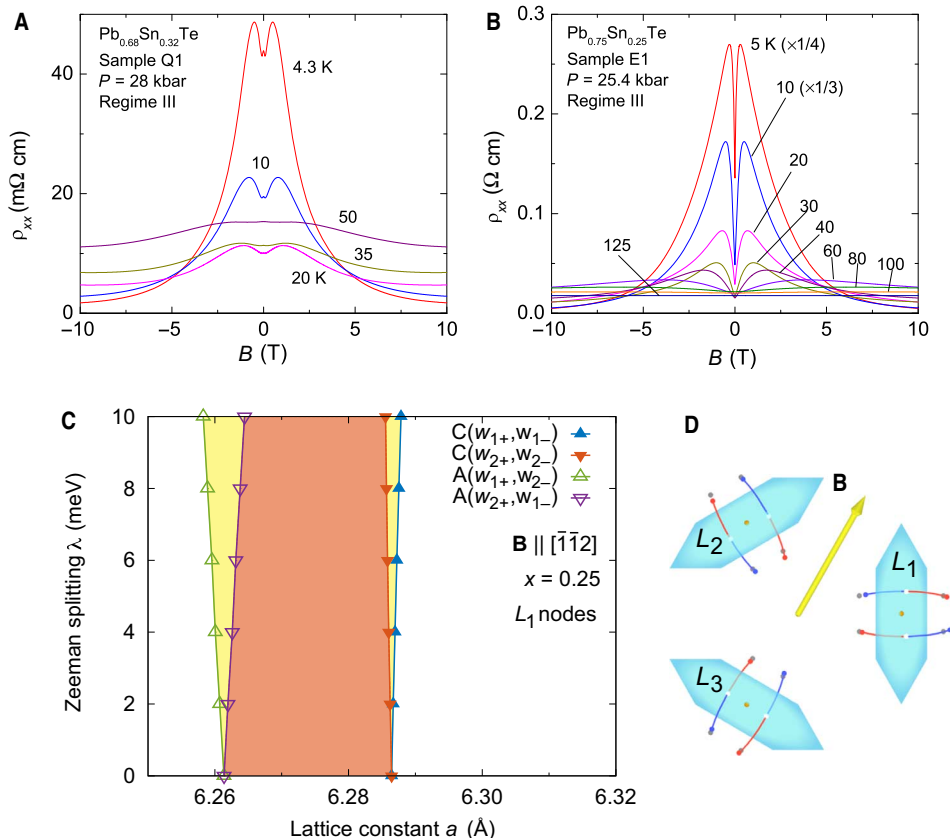


Fig. 4. Large, negative MR. A large isotropic MR is observed when P is fixed just above P_2 in samples Q1 and E1. (A) ρ_{xx} versus B in Q1 ($x = 0.32$) at selected T , with $P = 28$ kbar. At $P > P_2$, both samples are insulators at $B = 0$ T. However, at $B = 10$ T, both are metallic (ρ_{xx} decreases with T). In (B), similar curves show an even larger negative MR in sample E1 ($x = 0.25$). (C) *Ab initio* phase diagram (Supplementary Materials) in the plane of a versus λ at L_1 for $\mathbf{B} \parallel [\bar{1}\bar{1}2]$. With increasing λ , the Weyl node annihilation boundary (left V-shaped wedge shaded yellow) expands. A weaker expansion occurs at the creation boundary. (D) Effect of \mathbf{B} (yellow arrow) on the locations of the Weyl nodes around L_1 , L_2 , and L_3 .

A major difficulty in the rock salts is having to ensure that the chemical potential of the alloy lies within the bulk gap (otherwise, the pressure-induced changes to the gap will not be observable). To achieve this goal in crystals with Sn content $x = 0.5$, we have found it expedient to dope the starting material with indium [at the 6% level, with composition $(\text{Pb}_{0.5}\text{Sn}_{0.5})_{1-y}\text{In}_y\text{Te}$, with $y = 0.06$]. Indium doping has previously been carried out and investigated by several groups to understand the superconducting phase in $\text{Pb}_{1-x}\text{Sn}_x\text{Te}$ (17–19). Zhong *et al.* (19) have reported that In-doped $\text{Pb}_{1-x}\text{Sn}_x\text{Te}$ ($x = 0.5$) induces an insulating behavior. However, in our judgment, the precise role of In doping in the Pb-based rock salts is not well understood and merits further detailed investigation.

The x-ray diffractograms recorded for two powdered specimens of two typical samples are shown in fig. S4. The grown crystals were single-phased. The diffraction peaks were in very close agreement with the rock salt crystal structure of space group $Fm\bar{3}m$.

Some of the parameters measured in the four samples investigated (A1, A2, E1, and Q1) are reported in Table 1. The mobilities in E1 (p-type) and Q1 (n-type) were very high (500,000 and 4.2×10^6 cm^2/Vs , respectively). Although the samples with $x = 0.50$ (A1 and A2) had lower mobilities (18,000 and 29,000 cm^2/Vs , respectively), clear SdH oscillations were observed above P_1 .

Measurement of dielectric constant

We provide more details on the measurements of the relative dielectric constants ϵ_r . We adopted the (modified) Sawyer-Tower method (20, 21).

The circuit of the original Sawyer-Tower method is shown in Fig. 5A. Figure 5B shows the modified method using an operational amplifier (op-amp) (21).

For the setup shown in Fig. 5A, the sample with a capacitance component C_s and a resistance component R_s was connected in a series with a known reference capacitance $C_0 \gg C_s$. The reference capacitance C_0 was connected in parallel with a fixed resistor R_0 in series with an adjustable voltage source V_0 (or, equivalently, a variable resistor R_c) that was set such that the voltage V_y is inphase with voltage V_x , where V_x and V_y represent the voltages across the whole electrical circuit and the reference capacitor C_0 , respectively. Because $C_0 \gg C_s$ was satisfied, the following relations hold: $V_s \sim V_x$, $V_y \sim V_x C_s / C_0 \ll V_x$. Here, V_s is the voltage applied across the sample. This means that point M in the figure can be treated as a virtual ground. This yields the condition $V_0 / R_0 \sim V_s / R_s$.

The setup in Fig. 5B is the same as that in Fig. 5A except that the op-amp is used to provide a more stable virtual ground at point M. From point M, current I_F was driven to the op-amp connected to C_2 and R_2 in parallel. Here, a large resistor R_2 ($R_2 C_2 \gg 1/\omega$) was connected in parallel as the leak resistor so that the capacitor C_2 does not become overloaded. The integration circuit yielded the equation $V_y = C_2^{-1} \int I_F(t) dt$. If the adjustable voltage source V_1 is set to cancel the current I_s flowing into the sample, that is, if $V_1 / R_1 = V_x / R_s$ is satisfied, then the current I_F equals the current flowing into the capacitive component of the sample $I_s = dQ/dt = d(C_s V_x) / dt$. This gives $V_y = V_x C_s / C_2$, similar to the expression obtained for the case in Fig. 5A.

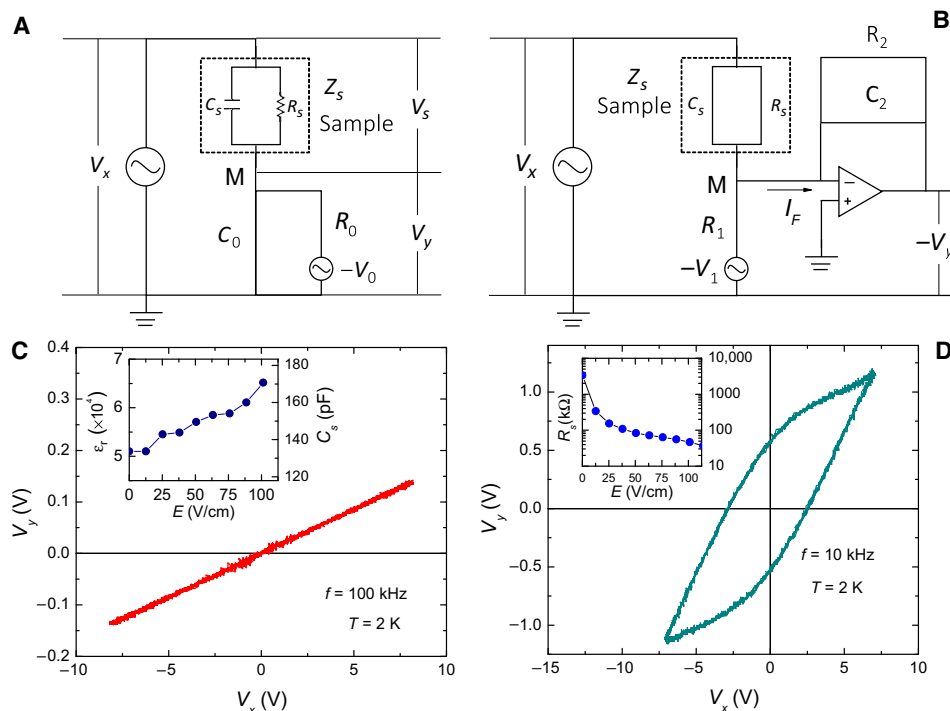


Fig. 5. Measurement of dielectric response. (A) Electrical circuit for measuring the relative dielectric constant ϵ_1 of the sample. The voltage $V_y \sim V_x C_s / C_0 < V_x$ is proportional to the dielectric displacement D . By contrast, the applied voltage V_x is proportional to the electrical field E in the sample. Therefore, the curve of V_x versus V_y gives the relation between E and D , yielding the relative dielectric constant ϵ_1 as a function of applied electric field E . (B) Modified electrical circuit of (A). The op-amp forces the point M to act as a virtual ground. The integration circuit yields $V_y = V_x C_s / C_2$ when the relation $V_1 / R_1 = V_x / R_s$ is satisfied. Because C_2 does not have to satisfy $C_2 \gg C_s$ in (B), a large value for V_y can be realized. (C) Curve relating E and D (V_x versus V_y), which yields a relative dielectric constant ϵ_1 as large as 5×10^4 even in the limit $E \rightarrow 0$ (inset). This implies that the system is in the FE state. (D) Apparent nonlinear relation between V_x and V_y caused by nonlinearity in the resistive component R_s of the sample. The inset shows how R_s varies with increasing E .

The advantage of using the op-amp is that one can choose any value of C_2 (as long the condition $R_2 C_2 \gg 1/\omega$ is satisfied) to attain a larger signal V_y than possible in the case in Fig. 5A. In general, the two setups in Fig. 5 (A and B) worked well. However, because the working frequency range of our op-amp (LF356N) was between 30 Hz and 30 kHz, we used setup A above 30 kHz. For frequencies below 30 kHz, both setups A and B were used. We confirmed that the two setups yielded the same results.

The measured results of the relative dielectric constants are plotted in Fig. 5C for $f = 100$ kHz and in Fig. 5D for $f = 10$ kHz. Figure 5C shows that $V_y = V_x C_s / C_2 = DS / C_2$ is proportional to $V_x = Et$. Here, E is the electric field in the sample, D is the dielectric displacement, and S and t are the area and the thickness of the sample, respectively. Using the values $S = 0.234$ mm² and $t = 0.79$ mm, we found the relative dielectric constants $\epsilon_1 \sim 5 \times 10^4$ (shown in the inset of Fig. 5C). Unfortunately, the sample suffered dielectric breakdown above $E \sim 100$ V/cm, which prevented us from observing the saturation of dielectric displacement D at higher electric fields as should be expected from the FE behavior. This large relative dielectric constant $\epsilon_1 \sim 5 \times 10^4$ observed in the limit $E \rightarrow 0$ strongly implies that the system is in the FE state.

We remark that the nonlinear behavior shown in Fig. 5D, previously interpreted by Möllmann *et al.* (22) as evidence for the FE state, is actually not the manifestation of the FE state. Rather, it arises from the fact that the resistive component of the sample R_s is strongly E -dependent, as shown in the inset. Because R_s is nonlinear, it is not possible to compensate the current I_s flowing through the resistive component R_s because $V_1 / R_1 = V_x / R_s$ cannot be satisfied for every V_x , unless V_1 is changed nonlinearly. Therefore, if V_1 is set to compensate the R_s at some

fixed value of V_x (7 V in the case of Fig. 5D), then other parts of V_x cannot be compensated. As a result, they produce a nonlinear behavior that looks like the saturation expected in the FE state. The way to avoid this is to use a higher frequency f so that a larger portion of the current flows into the capacitive component C_s rather than into the resistive component R_s . This is precisely the case shown in Fig. 5C ($f = 100$ kHz).

SUPPLEMENTARY MATERIALS

Supplementary material for this article is available at <http://advances.sciencemag.org/cgi/content/full/3/5/e1602510/DC1>

section S1. Ab initio band calculations

section S2. Field-induced anomalous Hall effect

fig. S1. Calculated \mathbf{k} -space trajectories of Weyl nodes in $\text{Pb}_{1-x}\text{Sn}_x\text{Te}$ ($x = 0.5$) under applied pressure in zero magnetic field.

fig. S2. Phase diagram of the Weyl phase in $\text{Pb}_{1-x}\text{Sn}_x\text{Te}$ ($x = 0.25$) and orbit parameters.

fig. S3. Phase diagram of the Weyl phase in $\text{Pb}_{1-x}\text{Sn}_x\text{Te}$ ($x = 0.25$) in the α - λ plane with applied $\mathbf{B} \parallel [112]$.

fig. S4. X-ray diffractograms of two powdered specimens of $\text{Pb}_{1-x}\text{Sn}_x\text{Te}$ taken from the crystal boules.

fig. S5. Supplemental data of $(\text{Pb}_{0.5}\text{Sn}_{0.5})_{1-y}\text{In}_y\text{Te}$ for samples A1 and A2.

fig. S6. Supplemental data of $\text{Pb}_{0.75}\text{Sn}_{0.25}\text{Te}$ for sample E1.

References (23–33)

REFERENCES AND NOTES

1. S. Murakami, Phase transition between the quantum spin Hall and insulator phases in 3D: Emergence of a topological gapless phase. *New J. Phys.* **9**, 356 (2007).
2. S. Murakami, S.-i. Kuga, Universal phase diagrams for the quantum spin Hall systems. *Phys. Rev. B* **78**, 165313 (2008).

3. R. Okugawa, S. Murakami, Dispersion of Fermi arcs in Weyl semimetals and their evolutions to Dirac cones. *Phys. Rev. B* **89**, 235315 (2014).
4. B.-J. Yang, N. Nagaosa, Classification of stable three-dimensional Dirac semimetals with nontrivial topology. *Nat. Commun.* **5**, 4898 (2014).
5. D. L. Mitchell, R. F. Wallis, Theoretical energy-band parameters for the lead salts. *Phys. Rev.* **151**, 581–595 (1966).
6. J. O. Dimmock, I. Melngailis, A. J. Strauss, Band structure and laser action in $\text{Pb}_{1-x}\text{Sn}_x\text{Te}$. *Phys. Rev. Lett.* **16**, 1193–1196 (1966).
7. B. A. Akimov, A. V. Dmitriev, D. R. Khokhlov, L. I. Ryabova, Carrier transport and non-equilibrium phenomena in doped PbTe and related materials. *Phys. Stat. Sol. A* **137**, 9–55 (1993).
8. L. Fu, Topological crystalline insulators. *Phys. Rev. Lett.* **106**, 106802 (2011).
9. T. H. Hsieh, H. Lin, J. Liu, W. Duan, A. Bansil, L. Fu, Topological crystalline insulators in the SnTe material class. *Nat. Commun.* **3**, 982 (2012).
10. P. Dziawa, B. J. Kowalski, K. Dybko, R. Buczko, A. Szczepaniak, M. Szot, E. Łusakowska, T. Balasubramanian, B. M. Wojek, M. H. Bernsten, O. Tjernberg, T. Story, Topological crystalline insulator states in $\text{Pb}_{1-x}\text{Sn}_x\text{Se}$. *Nat. Mater.* **11**, 1023–1027 (2012).
11. Y. Tanaka, Z. Ren, T. Sato, K. Nakayama, S. Souma, T. Takahashi, K. Segawa, Y. Ando, Experimental realization of a topological crystalline insulator in SnTe. *Nat. Phys.* **8**, 800–803 (2012).
12. S.-Y. Xu, C. Liu, N. Alidoust, M. Neupane, D. Qian, I. Belopolski, J. D. Denlinger, Y. J. Wang, H. Lin, L. A. Wray, G. Landolt, B. Slomski, J. H. Dil, A. Marcinkova, E. Morosan, Q. Gibson, R. Sankar, F. C. Chou, R. J. Cava, A. Bansil, M. Z. Hasan, Observation of a topological crystalline insulator phase and topological phase transition in $\text{Pb}_{1-x}\text{Sn}_x\text{Te}$. *Nat. Commun.* **3**, 1192 (2012).
13. Y. Okada, M. Serbyn, H. Lin, D. Walkup, W. Zhou, C. Dhital, M. Neupane, S. Xu, Y. J. Wang, R. Sankar, F. Chou, A. Bansil, M. Z. Hasan, S. D. Wilson, L. Fu, V. Madhavan, Observation of Dirac node formation and mass acquisition in a topological crystalline insulator. *Science* **341**, 1496–1499 (2013).
14. T. Liang, Q. Gibson, J. Xiong, M. Hirschberger, S. P. Koduvayur, R. J. Cava, N. P. Ong, Evidence for massive bulk Dirac fermions in $\text{Pb}_{1-x}\text{Sn}_x\text{Se}$ from Nernst and thermopower experiments. *Nat. Commun.* **4**, 2696 (2013).
15. L. J. Brillson, E. Burstein, L. Muldrew, Raman observation of the ferroelectric phase transition in SnTe. *Phys. Rev. B* **9**, 1547–1551 (1974).
16. N. Nagaosa, J. Sinova, S. Onoda, A. H. MacDonald, N. P. Ong, Anomalous Hall effect. *Rev. Mod. Phys.* **82**, 1539 (2010).
17. M. Novak, S. Sasaki, M. Kriener, K. Segawa, Y. Ando, Unusual nature of fully gapped superconductivity in In-doped SnTe. *Phys. Rev. B* **88**, 140502(R) (2013).
18. N. Haldolaarachchige, Q. Gibson, W. Xie, M. B. Nielsen, S. Kushwaha, R. J. Cava, Anomalous composition dependence of the superconductivity in In-doped SnTe. *Phys. Rev. B* **93**, 024520 (2016).
19. R. D. Zhong, J. A. Schneeloch, T. S. Liu, F. E. Camino, J. M. Tranquada, G. D. Gu, Superconductivity induced by In substitution into the topological crystalline insulator $\text{Pb}_{0.5}\text{Sn}_{0.5}\text{Te}$. *Phys. Rev. B* **90**, 020505(R) (2014).
20. C. B. Sawyer, C. H. Tower, Rochelle salt as a dielectric. *Phys. Rev.* **35**, 269–273 (1930).
21. T. Yamaguchi, M. Takashige, Key techniques of electric measurements of spontaneous polarization of ferro-electrics (in Japanese). *Butsuri* **66**, 603–609 (2011).
22. K.-P. Möllmann, K. H. Herrmann, R. Enderlein, Direct observation of ferroelectric phase in $\text{Pb}_{1-x}\text{Sn}_x\text{Te}$. *Physica B+C* **117–118**, 582–584 (1983).
23. G. Kresse, D. Joubert, From ultrasoft pseudopotentials to the projector augmented-wave method. *Phys. Rev. B* **59**, 1758 (1999).
24. G. Kresse, J. Furthmüller, Efficiency of ab-initio total energy calculations for metals and semiconductors using a plane-wave basis set. *Comput. Mater. Sci.* **6**, 15–50 (1996).
25. J. P. Perdew, A. Ruzsinszky, G. I. Csonka, O. A. Vydrov, G. E. Scuseria, L. A. Constantin, X. Zhou, K. Burke, Restoring the density-gradient expansion for exchange in solids and surfaces. *Phys. Rev. Lett.* **100**, 136406 (2008).
26. Y.-S. Kim, M. Marsman, G. Kresse, F. Tran, P. Blaha, Towards efficient band structure and effective mass calculations for III-V direct band-gap semiconductors. *Phys. Rev. B* **82**, 205212 (2010).
27. A. N. Mariano, K. L. Chopra, Polymorphism in some IV-VI compounds induced by high pressure and thin-film epitaxial growth. *Appl. Phys. Lett.* **10**, 282 (1967).
28. A. A. Mostofi, J. R. Yates, G. Pizzi, Y.-S. Lee, I. Souza, D. Vanderbilt, N. Marzari, An updated version of wannier90: A tool for obtaining maximally localised Wannier functions. *Comput. Phys. Commun.* **185**, 2309–2310 (2014).
29. R. Tsu, W. E. Howard, L. Esaki, Optical and electrical properties and band structure of GeTe and SnTe. *Phys. Rev.* **172**, 779 (1968).
30. J. Liu, D. Vanderbilt, Weyl semimetals from noncentrosymmetric topological insulators. *Phys. Rev. B* **90**, 155316 (2014).
31. J. O. Dimmock, *Physics of Semimetals and Narrow-Gap Semiconductors*, D. L. Carter, R. T. Bate, Eds. (Pergamon, 1971).
32. E. Ridolfi, E. A. de Andrada e Silva, G. C. La Rocca, Effective g -factor tensor for carriers in IV-VI semiconductor quantum wells. *Phys. Rev. B* **91**, 085313 (2015).
33. Z. Fang, N. Nagaosa, K. S. Takahashi, A. Asamitsu, R. Mathieu, T. Ogasawara, H. Yamada, M. Kawasaki, Y. Tokura, K. Terakura, The anomalous Hall effect and magnetic monopoles in momentum space. *Science* **302**, 92–95 (2003).

Acknowledgments

Funding: The experimental project was supported by the U.S. Army Research Office (W911NF-16-1-0116) and the Gordon and Betty Moore Foundation's Emergent Phenomena in Quantum Systems Initiative through grant GBMF4539 (to N.P.O.). R.J.C. acknowledges NSF–Materials Research Science and Engineering Center grant DMR 1420541 (crystal growth). N.K. was supported by NSF–Partnership for Research and Education in Materials grant DMR-1205734 (calculations) and the U.S. Army of Defense Grant number W911NF-16-1-0487 for the computer cluster. **Author contributions:** T.L. conceived the idea of applying pressure to PbSnTe and developed the experimental program with N.P.O. The samples were grown by S.K., Q.G., and R.J.C. The measurements were performed by T.L. with some assistance from J.L. Analyses of the results were performed by T.L., N.P.O., J.K., and N.K. The ab initio calculations were performed by J.K. and N.K. The manuscript was written by T.L. and N.P.O. with inputs from J.K. and N.K. **Competing interests:** The authors declare that they have no competing interests. **Data and materials availability:** All data needed to evaluate the conclusions in the paper are present in the paper and/or the Supplementary Materials. Additional data related to this paper may be requested from T.L. (liang16@stanford.edu) or N.P.O. (npo@princeton.edu).

Submitted 14 October 2016

Accepted 31 March 2017

Published 31 May 2017

10.1126/sciadv.1602510

Citation: T. Liang, S. Kushwaha, J. Kim, Q. Gibson, J. Lin, N. Kioussis, R. J. Cava, N. P. Ong, A pressure-induced topological phase with large Berry curvature in $\text{Pb}_{1-x}\text{Sn}_x\text{Te}$. *Sci. Adv.* **3**, e1602510 (2017).